Available online at www.sciencedirect.com

ScienceDirect

International Journal of Naval Architecture and Ocean Engineering 8 (2016) 1–12
http://www.journals.elsevier.com/international-journal-of-naval-architecture-and-ocean-engineering/

# Prediction of velocity and attitude of a yacht sailing upwind by computational fluid dynamics

Heebum Lee [a], Mi Yeon Park [b], Sunho Park [c,*], Shin Hyung Rhee [d]

[a] Department of Naval Architecture and Ocean Engineering, Seoul National University, Republic of Korea
[b] Daewoo Shipbuilding and Marine Engineering Co, Ltd., Republic of Korea
[c] Department of Ocean Engineering, Korea Maritime and Ocean University, Busan, 727 Taejong-ro, Yeongdo-gu, 606-791, Republic of Korea
[d] Department of Naval Architecture and Ocean Engineering, Research Institute of Marine Systems Engineering, Seoul National University, Republic of Korea

Received 6 July 2014; revised 13 October 2014; accepted 14 May 2015
Available online 18 January 2016

**Abstract**

One of the most important factors in sailing yacht design is accurate velocity prediction. Velocity prediction programs (VPP's) are widely used to predict velocity of sailing yachts. VPP's, which are primarily based on experimental data and experience of long years, however suffer limitations when applied in realistic conditions. Thus, in the present study, a high fidelity velocity prediction method using computational fluid dynamics (CFD) was proposed. Using the developed method, velocity and attitude of a 30 feet sloop yacht, which was developed by Korea Research Institute of Ship and Ocean (KRISO) and termed KORDY30, were predicted in upwind sailing condition.


*Keywords:* Computational fluid dynamics (CFD); Velocity prediction; Sailing attitude prediction; Sailing yacht

## 1. Introduction

General merchant ships obtain their propulsion force from propellers, but sailing yachts obtain their propulsion force from the action of the wind against the sail. Therefore, in sailing yachts, it is very important to optimize the aerodynamic performance of the sail, which converts the wind to propulsion force.

One of the most important goals in the design and development of a sailing yacht is to generate the propulsion force required for the yacht to move forward at the desired speed with a stable attitude, keeping a balance with water and wind powers applied to the hull above and below the free-surface, respectively, in diverse sailing conditions. The aerodynamic forces applied on the sail, such as the drag or lift force, make the hull heel over and produce a specific leeway angle, i.e., the heading angle of the centerline with respect to the advance direction. Accordingly, to predict the resistance accurately, the leeway and heel conditions of sailing yachts are considered. Because the propulsion force, attitude of the hull, and resistance are closely interrelated, the condition of balance between all external forces and the reaction force of the hull, for which the speed will be predicted, has to be found. The velocity prediction program (VPP) finds the balance between external forces and the reaction force of the hull, and predicts the sailing speed. It calculates the attitude and speed of a yacht according to the wind speeds and angles using principal particulars, Froude number, and experimental data such as drag and lift force coefficients. VPP's are powerful in predicting the performance of conventional yachts. However, it is difficult to predict the performance of yachts of new concepts, because of the different range of the principal particulars, Froude number, and other characteristics. Moreover, changes in the rudder angle, and stall on sail, rudder, or keel due to large angle of attack are not considered in VPP's. VPP's are quite effective

* Corresponding author. Tel.: +82 51 410 4329.
*E-mail address:* spark@kmou.ac.kr (S. Park).
Peer review under responsibility of Society of Naval Architects of Korea.

http://dx.doi.org/10.1016/j.ijnaoe.2016.01.003

**Nomenclature**

| | |
|---|---|
| $C_D$ | Drag force coefficient [−] |
| $C_{HM}$ | Heeling moment coefficient [−] |
| $C_L$ | Lift force coefficient [−] |
| $C_P$ | Pressure coefficient [−] |
| $C_{SF}$ | Side force coefficient [−] |
| $C_T$ | Thrust coefficient [−] |
| $C_{YM}$ | Yaw moment coefficient [−] |
| $e_a^{21}$ | Approximate relative error [−] |
| $e_{ext}^{21}$ | Extrapolated relative error [−] |
| $GCI_{fine}^{21}$ | Fine-grid convergence index [−] |
| $P$ | Pressure [$Pa$] |
| $p$ | estimated order of accuracy of the computational method [−] |
| $P_{ref}$ | Reference pressure [$Pa$] |
| $U$ | Apparent wind speed [$m/s$] |
| $\phi$ | Computational solution variable for uncertainty assessment [−] |
| $\phi_{ext}^{21}$ | Extrapolated value [−] |
| $\rho$ | Density [kg/m$^3$] |

with respect to time, but cannot consider the real-world environments because they are based on empirical formulas.

Many studies have been conducted to overcome the aforementioned limitations. In overcoming these shortcomings, CFD is one of the most powerful yet feasible solutions. By CFD, the exact hull and sail geometries are used, and aero- and hydro-dynamic characteristics are calculated directly. For high fidelity performance prediction of a yacht, therefore CFD is believed to be the design tool in the future. Jones and Korpus (2001) used CFD to calculate the aerodynamic force on the sail and the hydrodynamic force on the keel, and applied the results to the design to prove that CFD would enable the optimal sail and keel design. Levadou et al. (1998) interpreted the flow around the hull using CFD, considering the hull shape above the free-surface, trim, and flooding. Parolini and Quarteroni (2005) interpreted the aerodynamic pressure on the sail and the hydrodynamic pressure and the surrounding flow field on the keel using CFD. The resulting resistance was more reasonable than the test result. Gerhardt et al. (2011) developed unsteady thin airfoil theory and solved the interaction of yacht sails by potential flow-based code. Kim et al. (2010b) analyzed sail and hull separately using CFD and verified the design of a sailing yacht. Mylonas and Sayer (2012) studied hydrodynamic flow around a yacht keel by Large Eddy Simulation (LES) and Detached Eddy Simulation (DES) approaches. Characteristics of the flow such as separation, vortices, and wakes are well predicted. Biancolini et al. (2014) proposed a method to optimize the sail trim to keep maximizing the boat speed using CFD and Radial Basis Function (RBF) mesh morphing. Besides yacht performance, studies on the sail were done. Kim et al. (2010a) studied mechanical properties of a sail and Bak et al. (2013) calculated deformation of a sail using fluid–structure interaction (FSI). Most of the preceding studies were conducted under the assumption that the sailing speed was constant. There have been few extensive studies on the attitude and speed of a sailing yacht, which suggests that more of such studies are needed.

In the present study, ANSYS CFX was used for mesh generation and computations. The objectives were therefore (1) to develop an algorithm to predict the speed and attitude of a sailing yacht and (2) to apply the developed algorithm to a 30 ft-class yacht.

The paper is organized as follows. The description of the computational method is presented first, and this is followed by the problem description. The computational results are then presented and discussed. Finally, a summary and conclusions are provided.

## 2. Object sailing yacht

KORDY 30, a sloop-type 30 ft-class yacht, was selected as the object sailing yacht for the present study. It has a sail system that consists of a jib sail, a main sail, and a mast as shown in Fig. 1 and Table 1. The overall length of the yacht hull was 9.142 m. The main sail's height (L2), width (W2), and thickness were 11.41 m, 4.41 m, and $5 \times 10^{-4}$ m, respectively. For the jib sail, the height (L1) was 9.68 m, the width (W1) was 3.294 m, and the thickness was $5 \times 10^{-4}$ m. The sail was

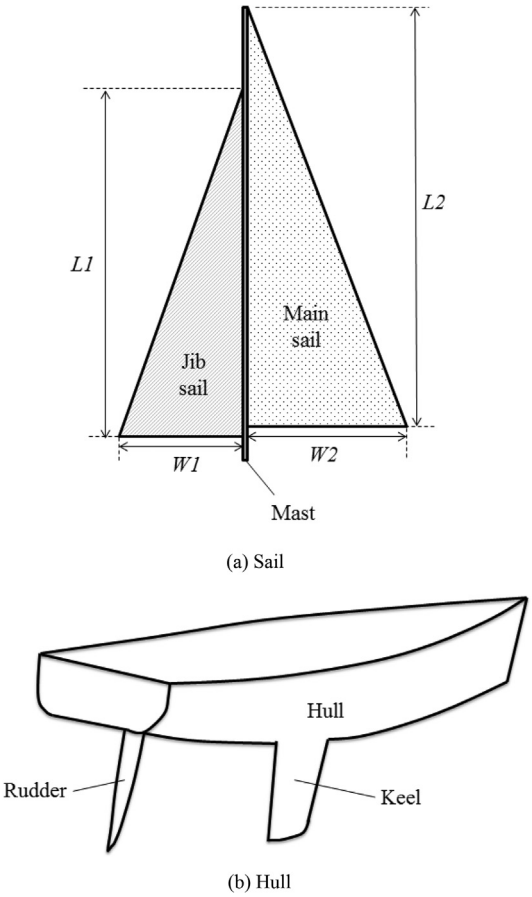


(a) Sail

(b) Hull

Fig. 1. KORDY 30.

Table 1
Principal particulars of KORDY 30.

| | Definition | Value |
|---|---|---|
| LOA (m) | Length Overall | 9.142 |
| LWL (m) | Water Line Length | 8.245 |
| B (m) | Beam | 3.024 |
| Tc (m) | Draft w/o Keel | 0.400 |
| T (m) | Draft with Keel | 1.900 |
| ∇ ($m^3$) | Displacement | 3.298 |
| Wetted surface area ($m^2$) | Hull | 15.600 |
| | Keel | 2.840 |
| | Rudder | 1.180 |

made of kevlar fiber, and its density was $1.44 \times 10^3$ kg/$m^3$. The Poisson ratio and the Young's modulus of the kevlar fiber were 0.36 and 83 GPa, respectively.

## 3. Computational methods

### 3.1. Algorithm for yacht speed and attitude prediction

When the external forces and reaction force of the hull balanced, the speed and attitude of a sailing yacht were predicted for constant wind speed and angle conditions. In this study, the performance prediction algorithm is revised to apply CFD for the speed prediction analysis based on the existing VPP algorithm as shown in Fig. 2. First, the apparent wind speed and angle were decided, and then the sailing speed, heel angle, leeway angle, and rudder angle were assumed. Second, the aerodynamic force and moment acting on the sail were calculated. Third, the hydrodynamic force and moment were calculated for the yacht hull below the free-surface. Fourth, the heeling moment and transverse righting moment were compared to update the heel angle. Fifth, the ratio of the thrust to the lateral sail force and the ratio of the resistance to the lateral hull force were calculated and compared to correct the leeway angle. Sixth, the yacht speed was decided by comparing the thrust with the resistance. Seventh, the yaw moment was comparatively examined, and if it was inconsistent, the rudder angle was adjusted. Finally, the balance between all external forces and the reaction force of the hull was calculated again, and if the result was inconsistent, the calculation was repeated from the first step, with the result as the previous step's.

### 3.2. Numerical methods

The mass conservation, momentum conservation, turbulence model, and volume fraction transport equations were solved. The time derivative term was discretized by the first-order accurate scheme. The cell-centered finite volume method was used, and the PISO algorithm was used for the velocity and pressure coupling. The second-order upwind scheme was used for the convection term, and the second-order central differencing scheme was used for the diffusion term. The flux evaluation term of the volume fraction equation was discretized using the high-order discretization method (Ubbink, 1996). The realizable $k$-$\varepsilon$ turbulence model with the wall function (Park et al., 2013) was considered. For the two-phase flow, the changes in the density and viscosity were calculated from the state equation. To accelerate convergence of the solution, the algebraic multi-grid (AMG) method was

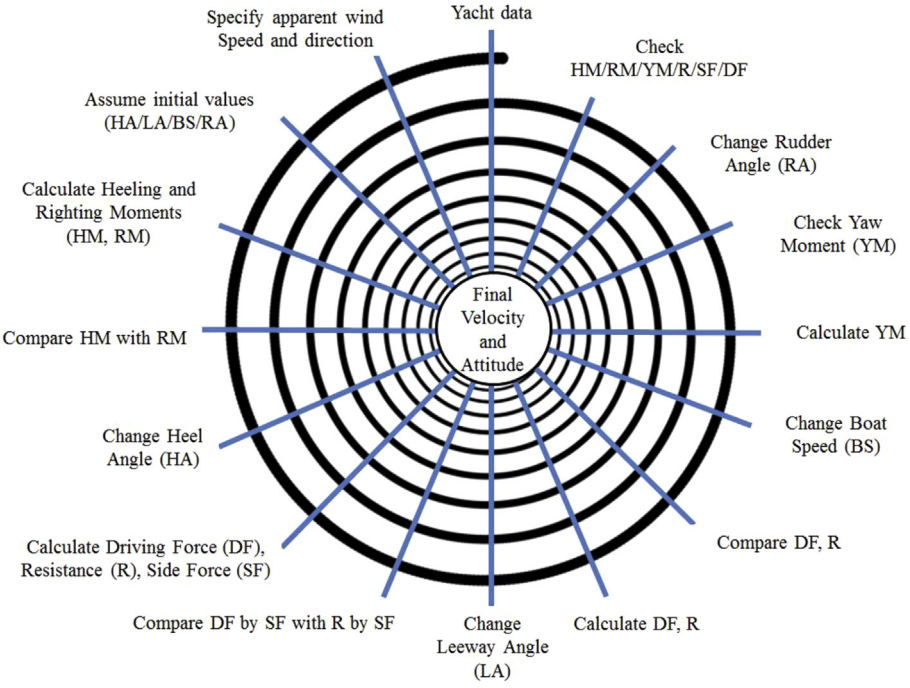


Fig. 2. Velocity prediction algorithm for CFD.

used along with the Gauss-Seidel iterative algorithm method. The computations were performed using the commercial CFD software ANSYS CFX.

### 3.3. Computational methods and boundary conditions

The aerodynamic force on the sail and the hydrodynamic force on the hull were computed separately. In other words, there were two computational domains; one included the sail and the other included the hull and keel.

The computational domain for the flow around the sail was trapezoid-shaped, as shown in Fig. 3, and its extent was 100 m−260 m wide, 170 m long, and 50 m high. Fig. 4 shows the mesh around the sails. There were 1.3 million structured cells in the subdomain surrounding the sails and approximately 640,000 structured cells in the external subdomain. A total of 1.95 million cells were placed in the entire domain. The Dirichlet-type boundary condition was imposed on the inlet, port and starboard sides as the inflow boundary surfaces, whereas the Neumann-type boundary condition was used for the downstream outlet as the outflow boundary surface. The wind incidence at the sail was set in seven cases at angles that ranged from 30° to 90° at a wind speed of 20 knots. The test conditions are listed in Table 2. When the wind angle was greater than 90°, a sailing yacht was generally equipped with a spinnaker or gennaker and sails downwind. The computation

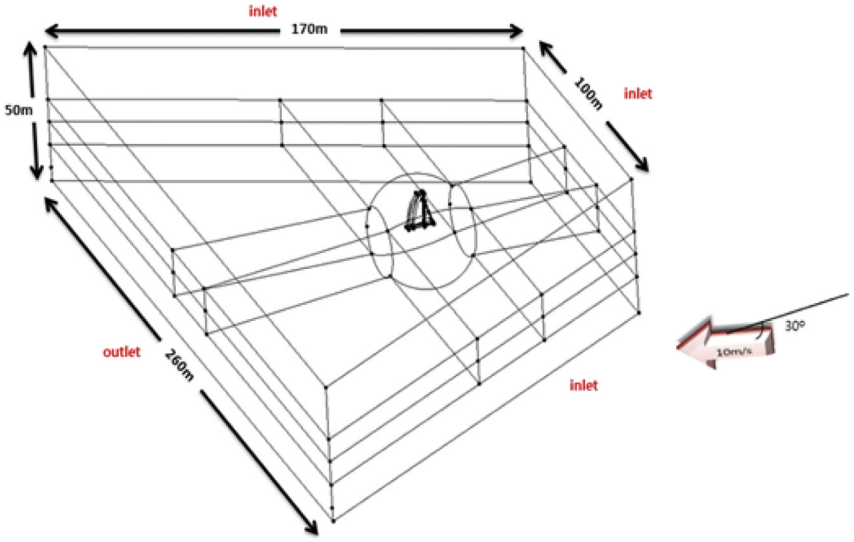


(a) Computational domain for Sails

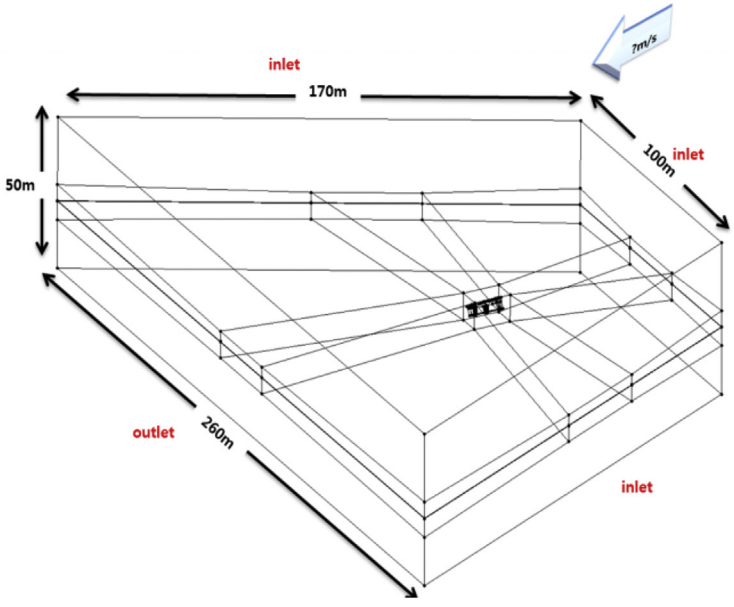


(b) Computational domain for hull and keel

Fig. 3. Domain extent.

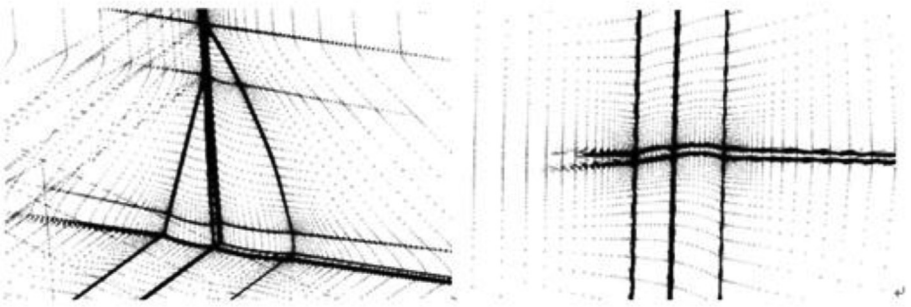

Fig. 4. Mesh around the sail.

Table 2
Test conditions.

| Apparent wind velocity | Apparent wind angle |
|---|---|
| 10 m/s | 30° |
| | 40° |
| | 50° |
| | 60° |
| | 70° |
| | 80° |
| | 90° |

was conducted toward wind angles of up to 90°, which is the upwind range because only upwind sailing was considered in the present study. The no-slip boundary condition was set for the sail surface, and the non-matching condition was used for the boundary between the inner-subdomain surrounding the sails and the outer-subdomain. The solution interface between the inner- and outer-subdomains was handled using the general grid interface (GGI) interpolation method.

The overall domain size for the flow around the hull was the same as that for the flow around the sails, and an approximately 3.4 million-cell mesh was used for the flow around the hull. The speed and angle of the inflow were the input conditions for the boundary surface. However, the sailing speed and leeway angle were actually the solution of the computations, so they were initially assumed, and the assumed values were updated through iterations using the aforementioned speed prediction algorithm to find the final values. Note that fine cells were concentrated near the free-surface to capture the free-surface precisely.

### 3.4. Uncertainty assessment

To evaluate the discretization errors, the procedure by Celik et al. (2008) for evaluating grid convergence index (GCI) was adopted. The computations were done for the side force with three different meshes with 7.66 ($N_1$), 3.4 ($N_2$) and 1.48 ($N_3$) million cells. The representative cell size $h$ for three-dimensional computations is calculated as

$$h = \left[\frac{1}{N}\sum_{i=1}^{N}(\Delta V_i)\right]^{1/3} \tag{1}$$

where $\Delta V_i$ is the volume of the $i$-th cell. The grid refinement factor ($r$), $h_{coarse}/h_{fine}$ was kept to be approximately 1.25.

The apparent order of accuracy can be estimated as

$$p = \frac{1}{\ln(r_{21})}\left|\ln\left|(\phi_3-\phi_2)/(\phi_2-\phi_1)\right| + q(p)\right| = \frac{1}{\ln(r_{21})}\left|\ln\left|\varepsilon_{32}/\varepsilon_{21}\right| + q(p)\right| \tag{2}$$

where

$$q(p) = \ln\left(\frac{r_{21}^{p} - 1\cdot sign(\varepsilon_{32}/\varepsilon_{21})}{r_{32}^{p} - 1\cdot sign(\varepsilon_{32}/\varepsilon_{21})}\right) \tag{3}$$

Here $\phi_1$, $\phi_2$, and $\phi_3$ are solutions at the coarse, medium, and fine levels, respectively. Negative values of $\varepsilon_{32}/\varepsilon_{21} < 0$ are an indication of oscillatory convergence. The extrapolated value is calculated as

$$\phi_{ext}^{21} = \left(r_{21}^{p}\phi_1 - \phi_2\right)/\left(r_{21}^{p} - 1\right) \tag{4}$$

Approximate relative error, extrapolated relative error, and fine-grid convergence index were calculated as, respectively,

$$e_a^{21} = \left|\frac{\phi_1 - \phi_2}{\phi_1}\right| \tag{5}$$

$$e_{ext}^{21} = \left|\frac{\phi_{ext}^{12} - \phi_1}{\phi_{ext}^{12}}\right| \tag{6}$$

$$GCI_{fine}^{21} = \frac{1.25e_a^{21}}{r_{21}^{p} - 1} \tag{7}$$

Table 3
Numerical uncertainty assessment.

| | $\phi$ = side force (N) |
|---|---|
| $N_1/N_2/N_3$ | 8,696,000/17,180,000/34,360,000 |
| $h_{21}/h_{32}$ | 1.25/1.26 |
| $\phi_1/\phi_2/\phi_3$ | 3076/3156/3200 |
| $P$ | 2.67 |
| $\phi_{ext}^{21}$ | 2980 |
| $e_a^{21}$ | 2.59% |
| $e_{ext}^{21}$ | 3.20% |
| $GCI_{fine}^{21}$ | 3.88% |

Table 3 summarizes the numerical uncertainty assessment results. Overall, the solutions show good mesh convergence behavior with errors from the corresponding extrapolated value of less than 4%.

## 4. Results and discussion

Fig. 5 shows the sail trim and hull attitude at 30°, 60° and 90° apparent wind angles. The forestay of the jib sail and the

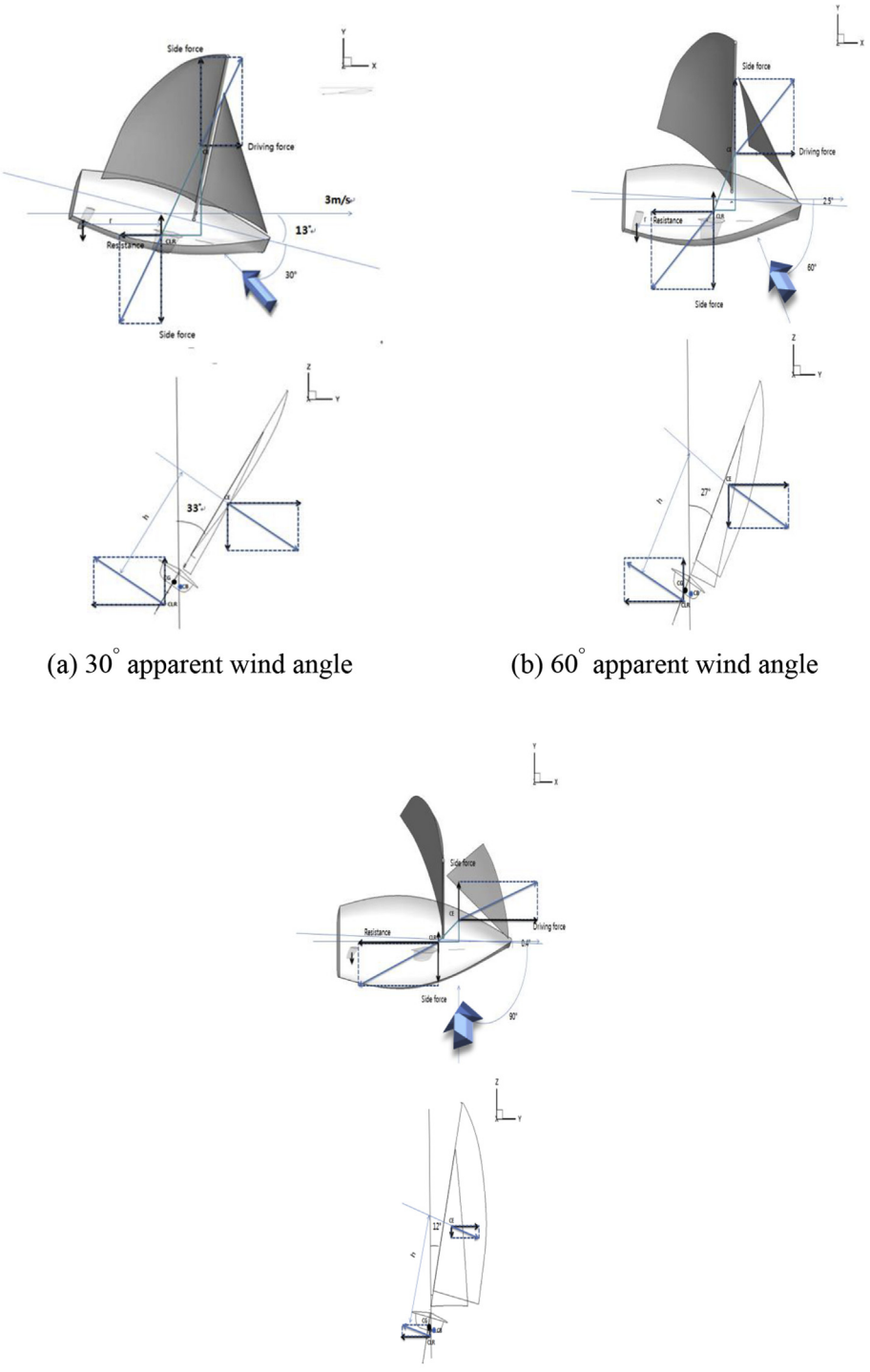


(a) 30° apparent wind angle

(b) 60° apparent wind angle

(c) 90° apparent wind angle

Fig. 5. Sail trim and yacht performance.

luff of the main sail were fixed, and the sail angle was changed according to the apparent wind angle. The heel, leeway, rudder angles were calculated from the equilibrium state for the moment determined by calculating the center of effect, to which the aerodynamic force on the yacht sail was applied, and the center of lateral resistance, to which the hydrodynamic force on the hull and keel was applied, separately. Table 4 lists the final sailing speed, and heel, leeway and rudder angles for various apparent angles. For small apparent angle, the attitude changed dramatically. The apparent angle of 90° shows the maximum sailing speed due to the maximum lift force of the sail.

All the computations for the apparent wind angles ranged from 30° to 90° were conducted until the balance between the aerodynamic and hydrodynamic forces was reached, and the error indicated the difference between the aerodynamic and hydrodynamic forces. To achieve the balance between the forces, at least three computations were cone for the hull and sails, respectively, in each iteration cycle. Until the equilibrium state, three cycles of computations were required. As listed in Table 5, all the forces had errors of 2.5% or less in all the cases. Fig. 6 shows the convergence history for the heeling and righting moments. After three cycles, the solutions were converged.

Table 4
Final speed and attitude.

| Apparent angle (deg.) | Sailing speed (m/s) | Heel angle (deg.) | Leeway angle (deg.) | Rudder angle (deg.) |
|---|---|---|---|---|
| 30 | 3 | 33 | 13 | 4 |
| 60 | 4.48 | 27 | 2.5 | 1.8 |
| 90 | 5.03 | 12 | 0.4 | 0.88 |

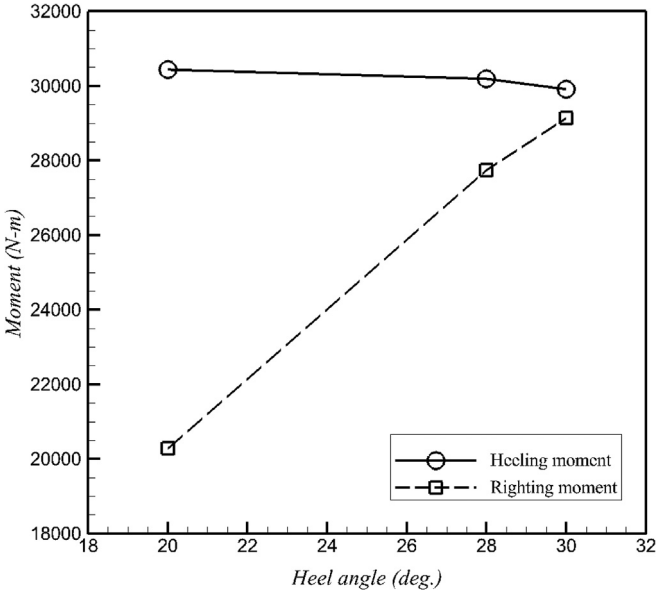


Fig. 6. Convergence history of heel angle.

It was important to estimate the force on the sail before analyzing the attitude of the sailing yacht. Fig. 7 shows the pressure coefficient distribution on the sail. The pressure coefficient ($C_{press} = (P - P_{ref})/0.5\rho U_{\infty}^2$) was non-dimensionalized by the reference pressure ($P_{ref}$), fluid density ($\rho$), and apparent winds ($U$). The lowest pressure was found on the forestay and foot of the jib and main sails. Because the pressure difference between the pressure and suction sides produced the lift force, the pressure coefficient distribution indicated that a greater apparent wind angle generated a greater lift force.

Table 5
Force and moment balance errors.

| Apparent wind angle (degree) | | Thrust resistance (N) | Side force (N) | Weight buoyancy (N) | Heeling moment/righting moment (N-m) | Yaw moment (N-m) |
|---|---|---|---|---|---|---|
| 30 | Sail | 1597.4 | 3344.7 | 34,156.5 | 28,159.1 | 6126.1 |
| | Hull | 1635.1 | 3326.6 | 33,472.0 | 28,586.5 | 6020.8 |
| | Difference (%) | 2.3 | 0.5 | 2.0 | 1.5 | 1.7 |
| 40 | Sail | 1897.6 | 3340.8 | 34,062.0 | 27,162.7 | 6715.3 |
| | Hull | 1868.0 | 3268.6 | 33,931.5 | 27,083.1 | 6640.0 |
| | Difference (%) | 1.6 | 2.2 | 0.4 | 0.3 | 1.1 |
| 50 | Sail | 2363.8 | 3151.6 | 34,033.9 | 25,007.9 | 7956.6 |
| | Hull | 2304.8 | 3163.3 | 34,290.6 | 25,018.6 | 7839.5 |
| | Difference (%) | 2.5 | 0.4 | 0.8 | 0.0 | 1.5 |
| 60 | Sail | 3006.3 | 2888.5 | 33,903.2 | 21,725.0 | 8523.3 |
| | Hull | 3036.2 | 2943.6 | 33,613.9 | 21,757.2 | 8430.2 |
| | Difference (%) | 1.0 | 1.9 | 0.9 | 0.2 | 1.1 |
| 70 | Sail | 3598.0 | 2622.5 | 32,918.2 | 1724.3 | 6436.5 |
| | Hull | 3569.7 | 2586.0 | 33,411.1 | 17,859.6 | 6330.7 |
| | Difference (%) | 0.8 | 1.4 | 1.5 | 1.9 | 1.7 |
| 80 | Sail | 4218.7 | 2167.2 | 32,501.9 | 14,010.9 | 4879.8 |
| | Hull | 4263.6 | 2182.1 | 32,209.8 | 14,306.6 | 4790.8 |
| | Difference (%) | 1.1 | 0.7 | 0.9 | 2.1 | 1.8 |
| 90 | Sail | 4489.1 | 1506.3 | 32,142.9 | 9968.5 | 3912.3 |
| | Hull | 4565.2 | 1518.4 | 31,629.3 | 10,088.3 | 3815.1 |
| | Difference (%) | 0.1 | 0.8 | 1.6 | 1.2 | 2.5 |

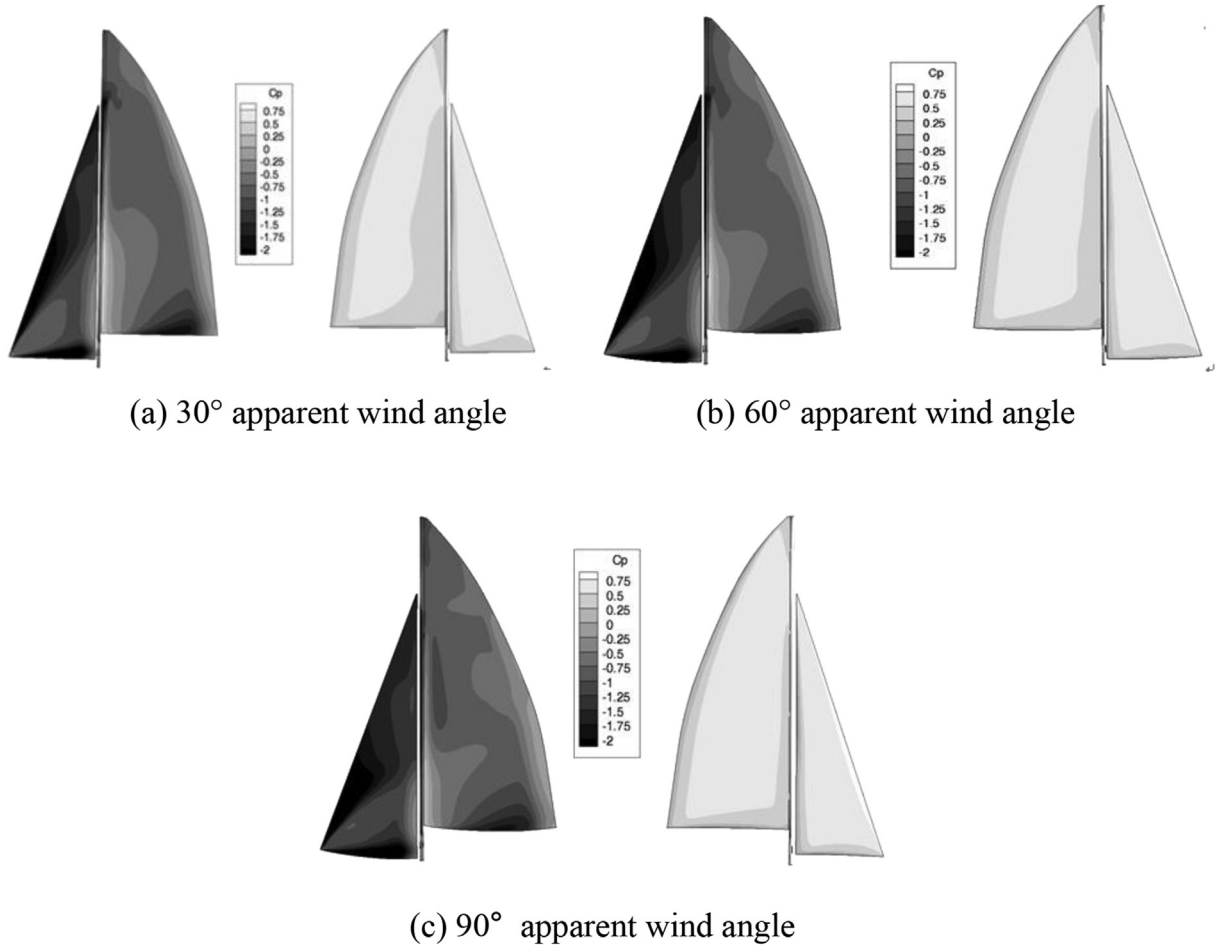


Fig. 7. Pressure coefficient contours.

Fig. 8 shows the lift and the drag force coefficients according to the apparent wind angles. A greater apparent wind angle increased the drag and lift forces. The increases in the drag and lift forces denoted the increase in the total resulting force. In Figs. 9 and 10, it is shown that the total resulting force increases, but the side force on the sail decreases. These indicated that the thrust increased more abruptly than the side force. Therefore, it could be said that a greater apparent wind angle increased the thrust of the sail and decreased the side force.

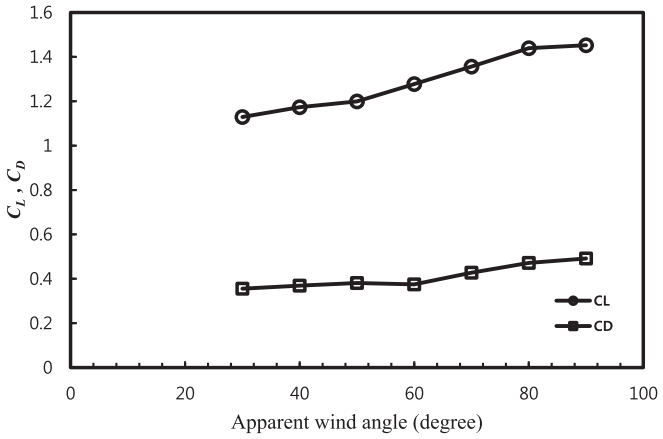


Fig. 8. Drag and lift force coefficients for various apparent wind angles.

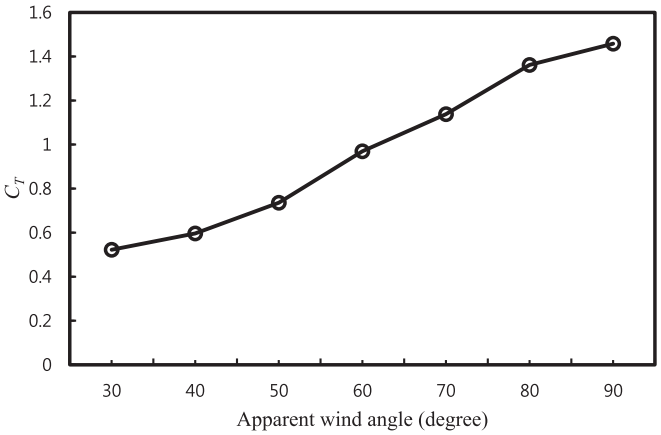


Fig. 9. Thrust coefficients for various apparent wind angles.

Table 6 presents the sailing speeds and heel, leeway, and rudder angles calculated according to the apparent wind angles. When the apparent wind angle increased, the side force applied to the sail decreased and thrust increased. The side

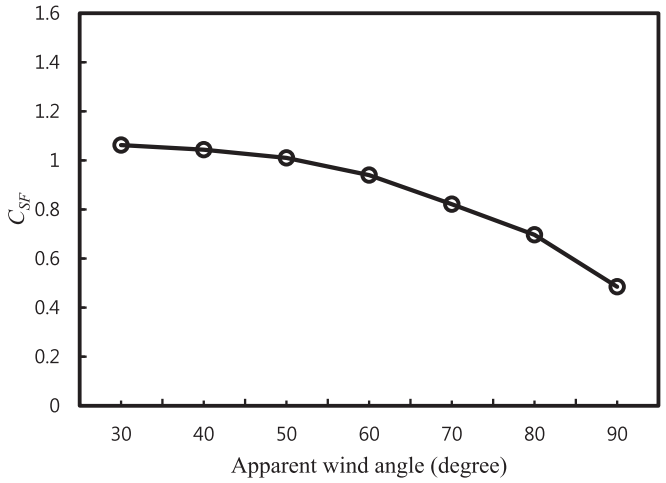


Fig. 10. Side force coefficients for various apparent wind angles.

Table 6
Heel angles, speeds, leeway angles, and rudder angles for various apparent wind angles.

| Apparent wind angle (°) | Heel angle (°) | Speed (m/s) | Leeway angle (°) | Rudder angle (°) |
|---|---|---|---|---|
| 30 | 33 | 3.00 | 13.00 | −4.00 |
| 40 | 31 | 3.65 | 7.00 | −1.70 |
| 50 | 30 | 4.02 | 4.50 | 0.00 |
| 60 | 27 | 4.45 | 2.50 | 1.80 |
| 70 | 22 | 4.65 | 1.40 | 1.85 |
| 80 | 17 | 4.94 | 0.95 | 0.90 |
| 90 | 12 | 5.03 | 0.40 | 0.88 |

force was proportional to the heel angle. The heel angle decreases with an increase of the apparent wind angle as shown in Fig. 11. The side force and thrust varied according to the difference in the heel angle, and in other words, the apparent wind angle and resulting sail trim changed the force on the sail. The side force was closely related to the heeling moment, and smaller side force indicated smaller heeling moment. Accordingly, the righting moment is small for large apparent wind angle, as shown in Fig. 12. From Figs. 11 and 12, a

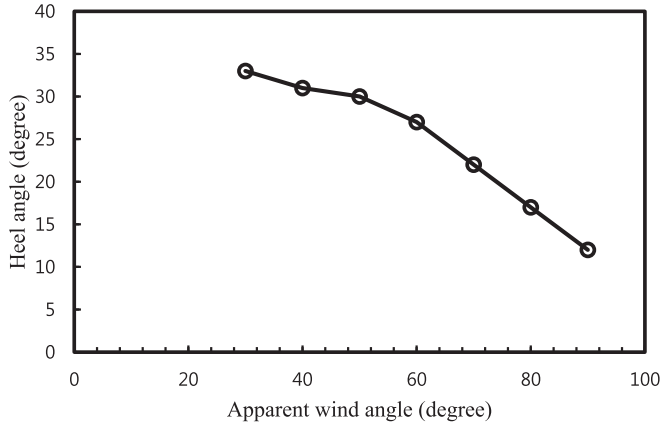


Fig. 11. Heel angles for various apparent wind angles.

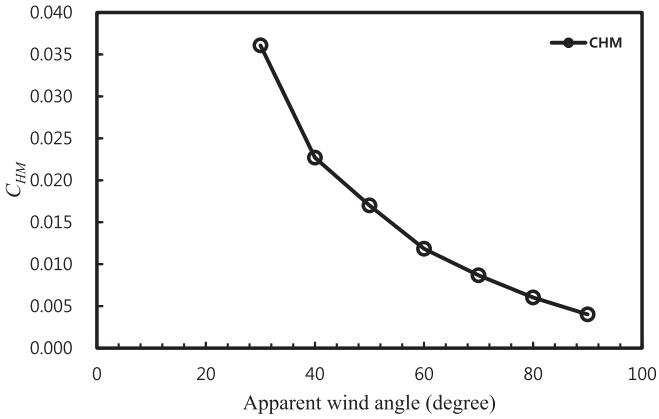


Fig. 12. Heeling moment coefficients for various apparent wind angles.

smaller heeling moment leads to a smaller heel angle for smaller righting moment.

Figs. 13 and 14 show the sailing speeds and leeway angles for various apparent winds, respectively. As the apparent wind angle increased, the sailing speed increased due to increasing thrust and the leeway angle, and decreased due to decreasing side force. The decreases in the heel and the leeway angles according to the apparent wind angles were related to the

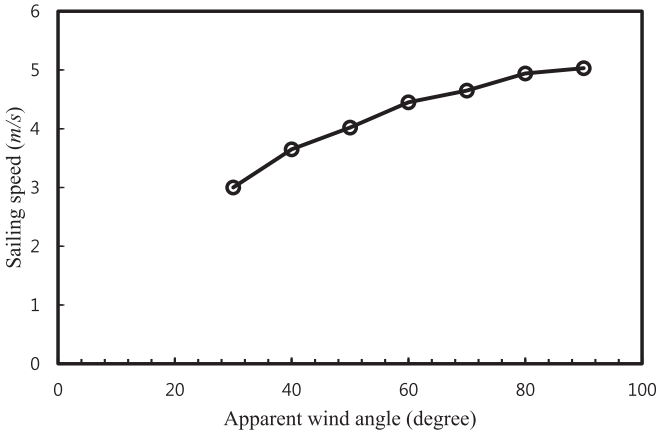


Fig. 13. Sailing speeds for various apparent wind angles.

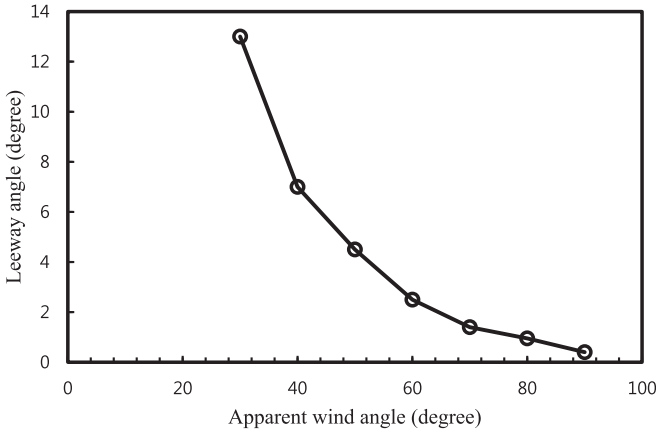


Fig. 14. Leeway angles for various apparent wind angles.

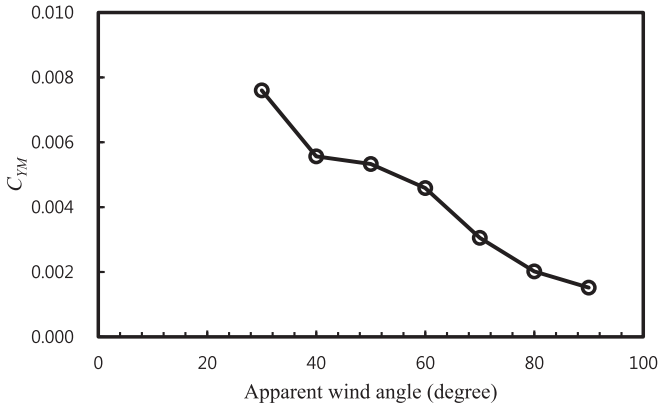


Fig. 15. Yaw moment coefficients for various apparent wind angles.

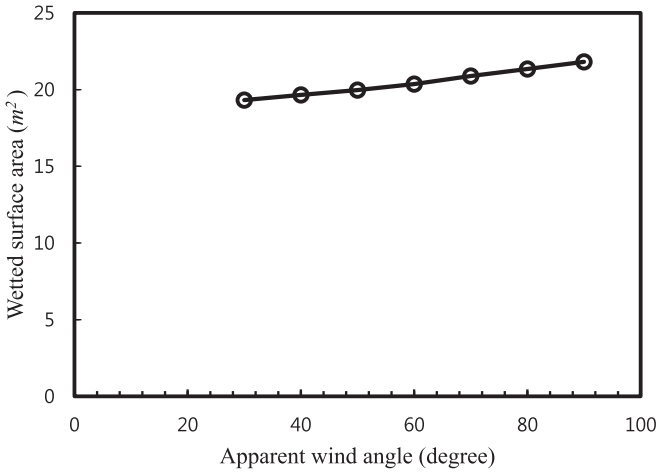


Fig. 17. Wetted surface areas for various apparent wind angles.

decrease in the yaw moment, as shown in Fig. 15, and the rudder angle was adjusted to ensure the balance of the yaw moment for sailing.

Because a sailing yacht sailed in the heeled attitude, the free-surface around the hull was not symmetric. Therefore, the rise and fall of the free-surface must be considered both sides of the hull. Fig. 16 shows the waterline according to the apparent wind angle. The waterline fell on the starboard side, but rose on the port side. When the apparent wind angle was smaller, the fall on the starboard side and the rise on the port side were clearer. Fig. 17 shows the wetted surface area according to the apparent wind angle. The heel angle caused decreasing wetted surface area. Thus, a greater apparent wind angle increased the wetted surface area.

Fig. 18 shows the pressure coefficient distribution on the hull and keel when the sailing yacht is in the equilibrium state. Because the attitude of the sailing yacht changed according to the apparent wind, the pressure distribution on the hull also changed. A sailing yacht had a heel and leeway angles for sailing balance, which changed the pressure distribution on the port and starboard sides of the hull, keel, and other surfaces. This generated the lift force that served as the force for the balance in the lateral angle. A greater apparent wind angle reduced the pressure (especially on the keel), because the decrease in the leeway angle reduced the incidence angle below the free-surface.

Table 7 lists the speed and attitude calculated by general VPP, which is based on IMS 2004 version (Offshore Racing Congress, 2004). It is observed that the heel and leeway angles are smaller than present computational results. In the CFD results presented, all the appendages were considered, while in the VPP results, the influences of rudder angle and other small appendages were ignored. Also, there are other factors than the hydro- and aerodynamic forces that determines the sailing attitude of a yacht.

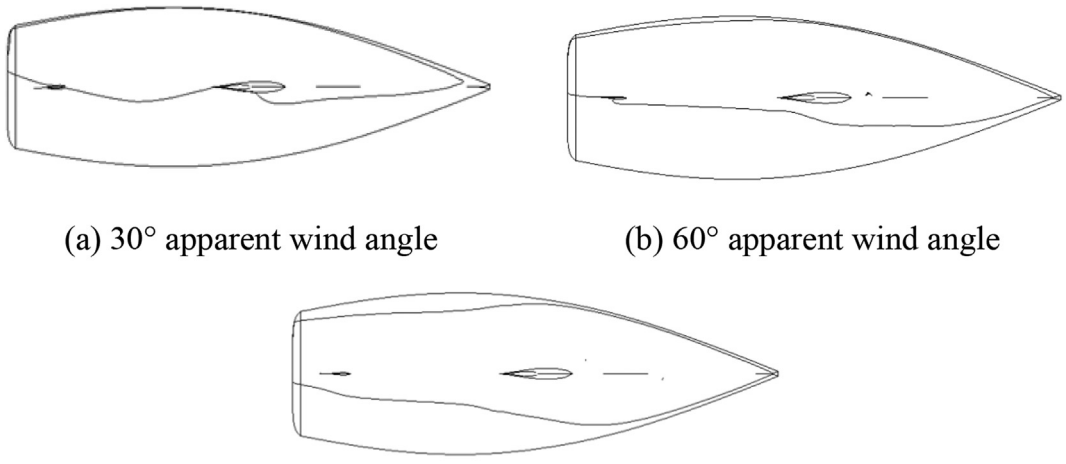


Fig. 16. Water line shape.

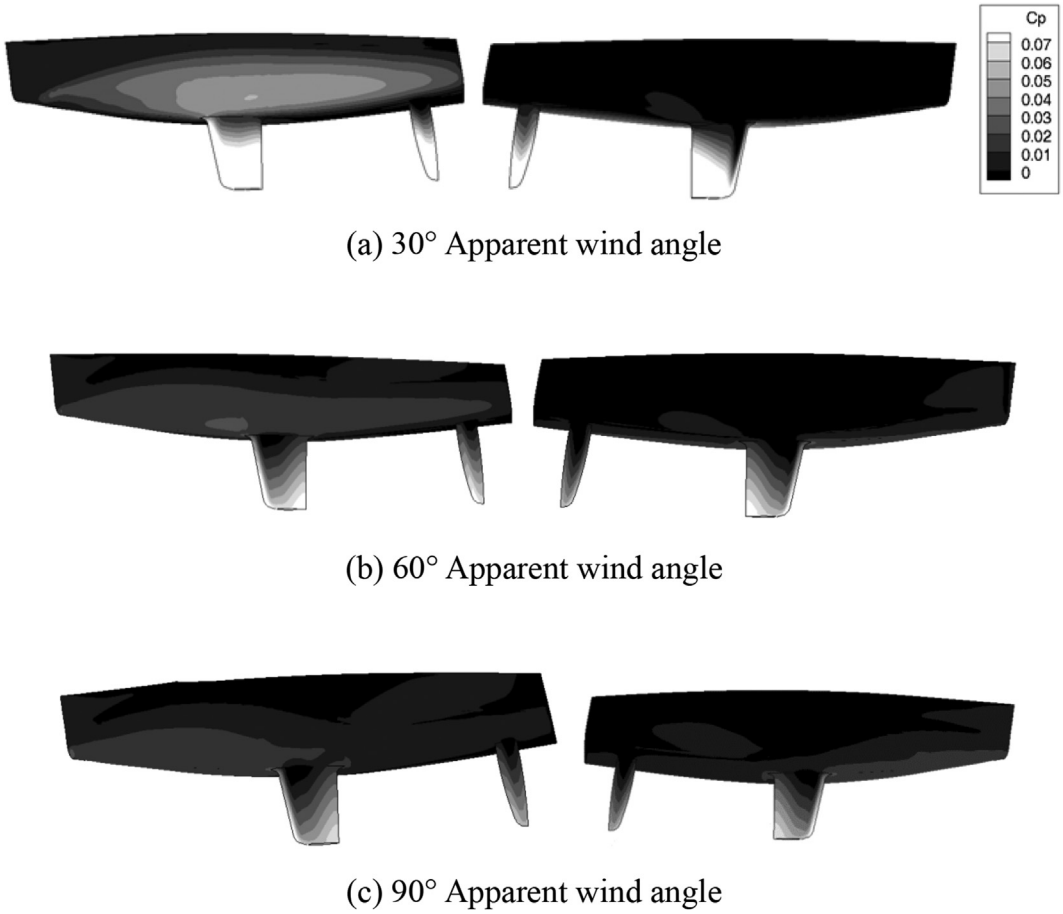


Fig. 18. Pressure coefficient contours at the port and starboard sides for 30° apparent wind angle.

Table 7
VPP results.

| Wind angle (deg.) | Sailing speed (m/s) | Heel angle (deg.) | Leeway angle (deg.) |
|---|---|---|---|
| 36.9 | 3.19 | 16.2 | 2.8 |
| 41.6 | 3.33 | 20.4 | 3.1 |

## 5. Concluding remarks

The algorithm for the prediction of the attitude and speed of a sailing yacht was established. The speed and angle of the sailing yacht changed until the balance of forces was reached for the constant wind speed and angle. Using the developed analysis algorithm, the speed and attitude of the sailing yacht were predicted.

The analysis for the prediction of the attitude and speed of a sailing yacht was conducted for a 30 ft-class sailing yacht with a hull, keel, and rudder. The results for seven cases with a 10 m/s wind speed and 30°, 40°, 50°, 60°, 70°, 80°, and 90° wind angles were comparatively investigated. A greater apparent wind angle increased the thrust of the sail and decreased the side force. As the apparent wind angle increased, the sailing speed increased due to increasing thrust and the leeway angle decreased due to decreasing side force. The decreases in the heel and the leeway angles according to the apparent wind angles were related to the decrease in the yaw moment.

In this paper, the forces and moments acting on the hull and sail were computed separately. Thus, the interaction of the hull and sail was considered in the one-way approach. For two-way interaction, computations for the hull and sail must be conducted together at the same time. As shown in Fig. 2, the moments were calculated first and then forces were compared next. To optimize the algorithm, sequence of each step should be changed by trial and error to get final velocity and attitude with minimum iteration. Additionally, it is widely acknowledged that sail deformation is one of the critical issues in determining the speed of sailing yacht. It is recommended that fluid–structure interaction (FSI) analysis be considered as future work.

## Acknowledgement

This work was supported by the National Research Foundation of Korea (2015037577, 2013R1A1A2012597) funded by the Ministry of Education of the Korea government, Multi-Phenomena CFD Research Center (20090093129) funded by

the Ministry of Science, ICT and Future Planning of the Korea government, and the IT R&D Program of MOTIE/KEIT (10060329).

## References

Bak, S., Yoo, J., Song, C.Y., 2013. Fluid-structure interaction analysis of deformation of sail of 30-foot yacht. Int. J. Nav. Archit. Ocean Eng. 5, 263−276.

Biancolini, M.E., Viola, I.M., Riotte, M., 2014. Sails trim optimisation using CFD and RBF mesh morphing. Comput. Fluids 93, 46−60.

Celik, I.B., Ghi, U., Roache, P.J., Freitas, C.J., Coleman, H., Raad, P.E., 2008. Procedure for estimation and reporting of uncertainty due to discretization in CFD applications. J. Fluids Eng. 130 (7), 078001.

Gerhardt, F.C., Flay, R.G.J., Richards, P., 2011. Unsteady aerodynamics of two interacting yacht sails in two-dimensional potential flow. J. Fluid Mech. 668, 551−581.

Jones, P., Korpus, R., 2001. America's cup class yacht design using viscous flow CFD. In: 15th Chesapeake Sailing Yacht Symposium, Annapolis, USA.

Kim, D., Hennigan, D.J., Beavers, K.D., 2010a. Effect of fabrication processes on mechanical properties of glass fiber reinforced polymer composites for 49 meter (160 foot) recreational yachts. Int. J. Nav. Archit. Ocean Eng. 2, 45−56.

Kim, W.-J., Yoo, J., Chen, Z., Rhee, S.H., Chi, H.-R., Ahn, H., 2010b. Hydro- and aero-dynamic analysis for the design of a sailing yacht. J. Mar. Sci. Technol. 15, 230−241.

Levadou, M.M.D., Prins, H.J., Raven, H.C., 1998. Application of advanced computational fluid dynamics in yacht design. In: 15th International Symposium on Yacht Design and Yacht Construction, Amsterdam, Netherlands.

Mylonas, D., Sayer, P., 2012. The hydrodynamic flow around a yacht keel based on LES and DES. Ocean. Eng. 46, 18−32.

Offshore Racing Congress, 2004. International Measurement System − a Handicapping System for Cruising/Racing Yachts. ORC Publications & Services.

Park, S., Park, S.W., Rhee, S.H., Lee, S.B., Choi, J.-E., Kang, S.H., 2013. Investigation on the wall function implementation for the prediction of ship resistance. Int. J. Nav. Archit. Ocean Eng. 5, 33−46.

Parolini, N., Quarteroni, A.L., 2005. Mathematical models and numerical simulations for the America's Cup. Comput. Methods Appl. Mech. Eng. 194, 1001−1026.

Ubbink, O., 1996. Numerical Prediction of Two Fluid Systems with Sharp Interface (Ph.D thesis). Imperial College of Science, Technology and Medicine.